On the scattering of a disk source by a rigid sphere for directivity broadening

Tim Mellow[1] and Leo Kärkkäinen[2,a] [iD]

[1]*Mellow Acoustics Ltd, 42 Hale Road, Farnham, Surrey GU9 9QH, United Kingdom*
[2]*Aalto University, Otakaari 1B, 02150 Espoo, Finland*

ABSTRACT:
The purpose of this study is to model a circular planar loudspeaker placed near a spherical reflector to broaden its directivity pattern, which would otherwise become increasingly narrow at high frequencies. Through ray tracing, it seems intuitively feasible to thus create a virtual point source at very high frequencies, but we provide a more rigorous analysis to determine what will happen at intermediate frequencies where the wavelength is of a similar magnitude to the diameter of the disk or sphere. We show that a smoother off-axis response is obtained with a dipole pressure source, which does not obstruct the scattered sound, rather than a monopole velocity source. Hence, an electrostatic loudspeaker, for example, would be more suitable than a dynamic one. The sphere may also serve as a spherical approximation of a human head, in which case the loudspeaker would become an open headphone that is not sealed to the ear. © 2022 Acoustical Society of America. https://doi.org/10.1121/10.0011732

I. INTRODUCTION

There is general agreement on the desirability for a loudspeaker to have a relatively constant directivity pattern over its working frequency range[1–3] because this ensures that the tonal balance of the reflected sound is as close as possible to that of the direct sound. Due to the precedence effect,[4] if the ear recognizes a reflected sound as correlating with the direct sound, it combines them into a single sound, which is then identified as coming from the direction of the original. Hence, the stereo image is reinforced, but this only works if the off-axis sound has a similar tonal balance to that on-axis.

This gives rise to the question of what kind of directivity pattern is most desirable to maintain over the working frequency range. From a practical point of view, it is difficult to achieve anything other than an omnidirectional pattern at the lowest frequencies. Dipole and cardioid patterns[5,6] have been employed but not without losing efficiency. Also, an omnidirectional pattern has subjective benefits at higher frequencies. Many musical instruments, such as strings and woodwinds, disperse the sound in all directions, albeit not as uniformly as a true monopole. Hence, the sound bounces off the walls, floor, and ceiling and immerses the listener in reflected sound. When this happens, the sound seems to float through the air creating a sense of spaciousness, even if the listening room is not an ideal performance venue.

There have been several methods for broadening the directivity pattern of a loudspeaker. One approach is to create a driver that imitates a pulsating sphere, such as the designs by Jürgen Reis[7] of MBL (Tokyo, Japan). Hiro Negishi[8] of Canon (Irvine, CA) designed a series of speakers that had conventional drivers firing down toward conical reflectors, and this approach has been revived by Hans van Maanen of Temporal Coherence (Huizen, Netherlands) but with the drivers firing upward toward the conical reflectors. Marcus Duevel employs a similar approach with various reflector shapes, including spheres. Peter Dicks of German Physiks (Maintal, Germany) prefers to use a vertically oscillating cone to radiate horizontally. To avoid reflectors or complicated driver configurations, phased arrays have been used by Peter Walker of Quad[9] and in the "oscillating sphere" concept by T.M.,[10] but these require more complicated electronics in the form of delay lines. In this paper, we focus on the simple spherical reflector, as shown in Fig. 1, as there appears to be little rigorous analysis of reflectors generally in the literature. Previous studies of spheres have been primarily focused on the scattering of the sound from a point source, rather than from a speaker diaphragm, for gaining insight into the head related transfer function (HRTF), either in the presence of a reflecting surface[11] or not,[12] or for the study of scattering in general.[13]

One of the reviews of this paper drew the attention of its authors to a paper by Zhong *et al.*,[14] which was published shortly after this one was submitted. Although Fig. 3 here looks very similar to Fig. 1 of Zhong *et al.*, the intentions of the two papers are quite different. The latter uses the sphere to represent the human head and how it affects the sound field produced by a parametric array loudspeaker (PAL) represented by the disk. Furthermore, it is assumed that the distance between the two is always larger than the wavelength, whereas this paper considers cases where the distance is greater or less than the wavelength.
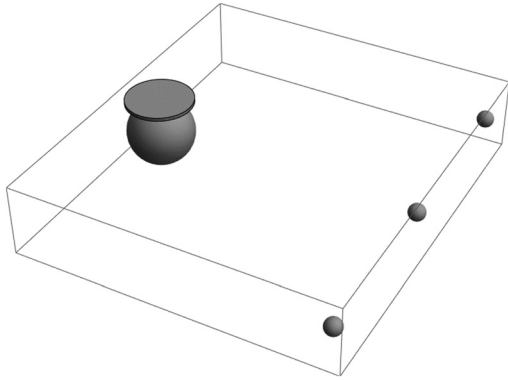
a)Electronic mail: leo.karkkainen@aalto.fi

FIG. 1. Disk and sphere in relation to three possible listening positions.

FIG. 2. Ray tracing of sound scattered from a disk by a sphere.

In Sec. II of this paper, we show how a virtual point source may be created from a disk and a sphere at high frequencies through simple ray tracing. After detailing the boundary conditions in Sec. III for a more rigorous analysis, we derive the near and far pressure fields for a resilient disk and sphere in Sec. IV and for a rigid disk and sphere in Sec. V. The dipole resilient disk in Sec. IV represents a disk of zero mass and stiffness driven by a uniform pressure distribution across its surface and can therefore be regarded as an idealized model for an electrostatic or planar magnetic transducer with a diaphragm in the form of a very light flexible membrane that is not clamped at its perimeter.

As well as plotting the far-field pressure of a loudspeaker with a spherical reflector, we plot the pressure between the transducer and the sphere whereby the sphere approximates the human head, and the transducer is an open headphone not sealed to the head. Unlike a conventional closed headphone with a rigid diaphragm, the resilient disk allows sound from within the ear to escape. In other words, there is no occlusion effect, which makes it more comfortable to wear.

By contrast, the monopole rigid disk in Sec. V represents two rigid back-to-back pistons that move in opposite directions to simply illustrate the fact that the flexible dipole transducer gives a smoother off-axis response than the rigid monopole one.

II. SIMPLE RAY-TRACING ANALYSIS

For simplicity, let us assume that the disk and sphere both have radius a and that the center of the disk meets the surface of the sphere, although in reality there would need to be a small gap to allow the disk to vibrate. Such a scheme is shown in Fig. 2. Let us also assume that the wavelength is so small that we may use ray tracing to predict how the sound emanating from the surface of the disk at a distance w_0 from its center will be scattered. We see from Fig. 2 that the angle of incidence and reflection from the sphere are both at an angle α from the normal, which itself is at an angle of α from the z axis or axis of rotational symmetry. Hence, the scattered sound subtends an angle $\theta = 2\alpha$ to the z axis, which is given by

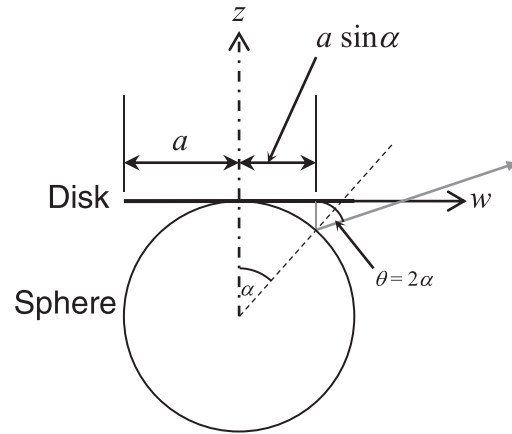$$\theta = 2\alpha = 2\arcsin(w/a). \tag{1}$$

Consequently, as the radial distance w varies from 0 to a, the angle θ varies from $0°$ to $180°$, which in turn means that the presence of the sphere converts the disk from a highly directive radiator at high frequencies to an omnidirectional one.

To put this in a more formal description, we assume that at very high frequencies, the sound from the disk travels as a plane wave toward the sphere such that the total volume velocity of the disk is incident upon the hemisphere facing the disk. For simplicity, we ignore the phase differences due to the increasing distance between disk and sphere along the radius, which will simply lead to corresponding phase differences in the directivity pattern. Hence, each volume velocity element of the disk is mapped onto the sphere as follows:

$$\begin{aligned}\delta\tilde{U}_{disk} &= \tilde{u}_0\delta S_{disk} \\ &= \delta\tilde{U}_{incident} = \tilde{u}_0\cos\alpha\delta S_{sphere},\end{aligned} \tag{2}$$

where the elemental areas of the disk and sphere are given, respectively, by

$$\delta S_{disk} = w\delta w\delta\phi, \tag{3}$$

$$\delta S_{sphere} = a^2\sin\alpha\delta\alpha\delta\phi. \tag{4}$$

Hence, we can write the incident volume velocity as

$$\begin{aligned}\tilde{U}_{disk} &= \tilde{u}_0\int_0^{2\pi}\int_0^a wdwd\phi = \pi a^2\tilde{u}_0 \\ &= \tilde{U}_{incident} = \tilde{u}_0 a^2\int_0^{2\pi}\int_0^{\pi/2}\cos\alpha\sin\alpha d\alpha d\phi.\end{aligned} \tag{5}$$

The reflected volume velocity is obtained by substituting $\alpha = \theta/2$ so that

$$\begin{aligned}\tilde{U}_{reflected} &= \tilde{u}_0\frac{a^2}{2}\int_0^{2\pi}\int_0^{\pi}\cos\left(\frac{\theta}{2}\right)\sin\left(\frac{\theta}{2}\right)d\theta d\phi \\ &= \tilde{u}_0\frac{a^2}{4}\int_0^{2\pi}\int_0^{\pi}D(\theta)\sin\theta d\theta d\phi = \tilde{u}_0\pi a^2,\end{aligned} \tag{6}$$

where $D(\theta)$ is the directivity function given by

J. Acoust. Soc. Am. **151** (6), June 2022

Tim Mellow and Leo Kärkkäinen   4115

$$D(\theta) = \frac{2}{\sin\theta}\cos\left(\frac{\theta}{2}\right)\sin\left(\frac{\theta}{2}\right) = 1. \tag{7}$$

Hence, the pattern is that of an omnidirectional point source. The purpose of this paper is to verify this hypothesis using more rigorous formulation that is applicable across the whole range of frequencies rather than just at the very highest. We will examine two cases: In the first, we have a dipole resilient disk, which is a disk of zero mass and stiffness driven by a uniform pressure distribution across its surface. In the second, we have a monopole disk in the form of two back-to-back pistons that move in opposite directions. Although this is an unlikely configuration, compared say to a piston at the end of a tube, it simplifies the analysis somewhat. We would expect the asymptotic low-frequency directivity patterns to be a figure-8 for the former and omnidirectional for the latter because the waves will simply diffract around the sphere. Also, we postulate that at high frequencies, both will become omnidirectional according to Fig. 2. A second purpose of this paper is to examine what will happen at frequencies in between, where the wavelength is of a similar magnitude to the circumference of the sphere. One advantage of the resilient disk is that it is acoustically transparent, which means that reflected waves will pass straight through it, whereas we would expect the rigid monopole disk to produce secondary reflections that interfere with the first ones.

III. BOUNDARY CONDITIONS

The loudspeaker is represented by a disk of radius a, as shown in Fig. 3. The center of the sphere of radius R lies at an axial distance d from the center of the disk, which lies at the origin of the axisymmetric cylindrical coordinate system (w, z), where w is the radial coordinate and z is the axial coordinate.

According to the Huygens–Fresnel principle, let the sound produced by each element of the disk be due to a point source of volume velocity $\tilde{U}_0$. The tilde denotes the missing factor $e^{j\omega t}$, where t is time, $\omega = 2\pi f = kc = 2\pi c/\lambda$ is the angular frequency, f is the frequency, k is the
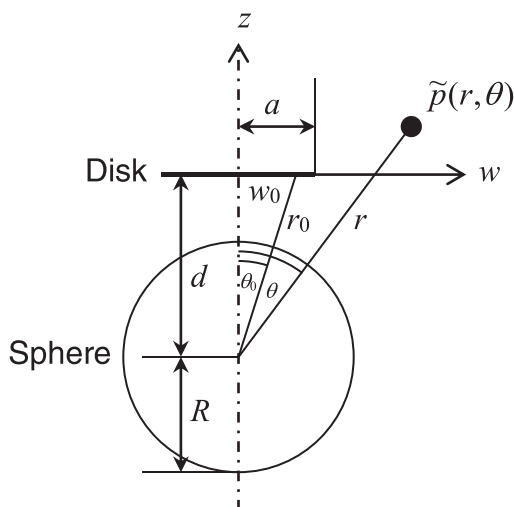

FIG. 3. Geometry of disk and sphere.

wavenumber, $c = 345$ m/s is the speed of sound, and λ is the wavelength. The incident field due to a point source is[10]

$$\tilde{p}_I(r, \theta) = \begin{cases} \dfrac{k^2\rho_0 c}{4\pi}\tilde{U}_0\displaystyle\sum_{n=0}^{\infty}(2n+1)j_n(kr_0)h_n^{(2)}(kr) \\ \quad\times P_n(\cos\theta_0)P_n(\cos\theta), \quad r > r_0 \\ \dfrac{k^2\rho_0 c}{4\pi}\tilde{U}_0\displaystyle\sum_{n=0}^{\infty}(2n+1)h_n^{(2)}(kr_0)j_n(kr) \\ \quad\times P_n(\cos\theta_0)P_n(\cos\theta), \quad r < r_0, \end{cases} \tag{8}$$

and the scattered field is

$$\tilde{p}_S(r, \theta) = -\frac{k^2\rho_0 c}{4\pi}\tilde{U}_0\sum_{n=0}^{\infty}(2n+1)\frac{j_n'(kR)}{h_n'^{(2)}(kR)} \\ \times h_n^{(2)}(kr_0)h_n^{(2)}(kr)P_n(\cos\theta_0)P_n(\cos\theta), \tag{9}$$

where

$$h_n^{(2)}(kR) = j_n(kR) - iy_n(kR), \tag{10}$$

$$j'_n(kR) = \frac{\partial}{\partial r}j_n(kr)|_{r=R} \\ = \frac{k}{2n+1}(nj_{n-1}(kR) - (n+1)j_{n+1}(kR)), \tag{11}$$

$$h_n'^{(2)}(kR) = \frac{\partial}{\partial r}h_n^{(2)}(kr)|_{r=R} \\ = \frac{k}{2n+1}\left(nh_{n-1}^{(2)}(kR) - (n+1)h_{n+1}^{(2)}(kR)\right), \tag{12}$$

and j_n and y_n are the spherical Bessel functions of the first and second kinds, respectively. Hence, the resultant pressure may be expressed as

$$\tilde{p}(r, \theta) = \tilde{p}_I(r, \theta) + \tilde{p}_S(r, \theta) \\ = ik\rho_0 c\tilde{U}_0 G(r, \theta|r_0, \theta_0), \tag{13}$$

where the uppercase G denotes the bounded Green's function given by

$$G(r, \theta|r_0, \theta_0) \\ = \frac{-ik}{4\pi}\sum_{n=0}^{\infty}(2n+1)P_n(\cos\theta_0)P_n(\cos\theta) \\ \times \begin{cases} \left(j_n(kr_0) - \dfrac{j_n'(kR)}{h_n'^{(2)}(kR)}h_n^{(2)}(kr_0)\right)h_n^{(2)}(kr), & r > r_0 \\ \left(j_n(kr) - \dfrac{j_n'(kR)}{h_n'^{(2)}(kR)}h_n^{(2)}(kr)\right)h_n^{(2)}(kr_0), & r \leq r_0. \end{cases} \tag{14}$$

IV. RESILIENT DISK

A. Calculation of the near-field pressure for the resilient disk

An electrostatic loudspeaker is represented by a resilient disk in which we assume that the diaphragm mass and

compliance are negligible. Hence, we model it as a harmonically varying driving pressure $\tilde{p}_0$ distributed uniformly over the surface of the disk. The near-field pressure due to the resilient disk, which is a dipole pressure source, is given by the dipole Rayleigh integral[10]

$$\tilde{p}(r,\theta) = \tilde{p}_0 \int_0^{2\pi} \int_0^a \frac{\partial}{\partial z_0} G(r,\theta|r_0,\theta_0)\Bigg|_{\substack{r_0=\sqrt{w_0^2+d^2} \\ \cos\theta_0 = d/r_0}} w_0 dw_0 d\phi_0,$$

(15)

where

$$\frac{\partial}{\partial z_0} = \frac{\partial r_0}{\partial z_0} \cdot \frac{\partial}{\partial r_0} + \frac{\partial \theta_0}{\partial z_0} \cdot \frac{\partial}{\partial \theta_0},$$

(16)

$$\frac{\partial r_0}{\partial z_0} = \cos\theta_0,$$

(17)

$$\frac{\partial \theta_0}{\partial z_0} = -\frac{\sin\theta_0}{r_0}.$$

(18)

Then

$$\frac{\partial}{\partial z_0} G(r,\theta|r_0,\theta_0)\Big|_{r>r_0}$$

$$= \frac{-ik}{4\pi} \sum_{n=0}^{\infty} (2n+1) h_n^{(2)}(kr) P_n(\cos\theta)$$

$$\times \Bigg\{ \left(j'_n(kr_0) - \frac{j'_n(kR)}{h_n'^{(2)}(kR)} h_n'^{(2)}(kr_0) \right) \cos\theta_0 P_n(\cos\theta_0)$$

$$- \frac{1}{r_0} \left(j_n(kr_0) - \frac{j'_n(kR)}{h_n'^{(2)}(kR)} h_n^{(2)}(kr_0) \right) \sin\theta_0 P'_n(\cos\theta_0) \Bigg\},$$

(19)

$$\frac{\partial}{\partial z_0} G(r,\theta|r_0,\theta_0)\Big|_{r\leq r_0}$$

$$= \frac{-ik}{4\pi} \sum_{n=0}^{\infty} (2n+1) \left(j_n(kr) - \frac{j'_n(kR)}{h_n'^{(2)}(kR)} h_n^{(2)}(kr) \right) P_n(\cos\theta)$$

$$\times \Bigg\{ h_n'^{(2)}(kr_0) \cos\theta_0 P_n(\cos\theta_0)$$

$$- \frac{1}{r_0} h_n^{(2)}(kr_0) \sin\theta_0 P'_n(\cos\theta_0) \Bigg\},$$

(20)

where

$$P'_n(\cos\theta_0) = \frac{\partial}{\partial\theta_0} P_n(\cos\theta_0)$$

$$= \frac{n(n+1)}{(2n+1)\sin\theta_0} (P_{n+1}(\cos\theta_0) - P_{n-1}(\cos\theta_0)).$$

(21)

Letting $w_0 = \sqrt{r_0^2 - d^2}$ and $r_0 = at$ in Eq. (15) yields

$$\tilde{p}(r,\theta)$$

$$= \frac{ka}{2}\tilde{p}_0 \sum_{n=0}^{\infty} i^{-n} P_n(\cos\theta)$$

$$\times \begin{cases} I_n^+(ka) h_n^{(2)}(kr), & r > \sqrt{a^2+d^2} \\ I_n^-(ka)\left(j_n(kr) - \dfrac{j'_n(kR)}{h_n'^{(2)}(kR)} h_n^{(2)}(kr) \right), & r \leq \sqrt{a^2+d^2} \end{cases},$$

(22)

where

$$I_n^+(ka) = i^{n-1} \int_{d/a}^{\sqrt{1+d^2/a^2}} \Bigg\{ \frac{d}{a}(2n+1)$$

$$\times \left(j'_n(kat) - \frac{j'_n(kR)}{h_n'^{(2)}(kR)} h_n'^{(2)}(kat) \right) P_n\left(\frac{d}{at}\right)$$

$$- n(n+1)\left(j_n(kat) - \frac{j'_n(kR)}{h_n'^{(2)}(kR)} h_n^{(2)}(kat) \right)$$

$$\times \left(P_{n+1}\left(\frac{d}{at}\right) - P_{n-1}\left(\frac{d}{at}\right) \right) \Bigg\} dt,$$

(23)

$$I_n^-(ka) = i^{n-1} \int_{d/a}^{\sqrt{1+d^2/a^2}} \Bigg\{ \frac{d}{a}(2n+1) h_n'^{(2)}(kat) P_n\left(\frac{d}{at}\right)$$

$$- n(n+1) h_n^{(2)}(kat)\left(P_{n+1}\left(\frac{d}{at}\right) - P_{n-1}\left(\frac{d}{at}\right) \right) \Bigg\} dt.$$

(24)

These integrals are evaluated as summations in the Appendix.

B. Near-field pressure plots for the resilient disk and comments

Figure 4 shows the on-axis pressure at different positions in the gap between the sphere and the disk, where both have the same diameters, and the gap is one-twentieth of the diameter of the sphere. The smoothest response is on the surface of the sphere (solid black trace), while the most irregular is on
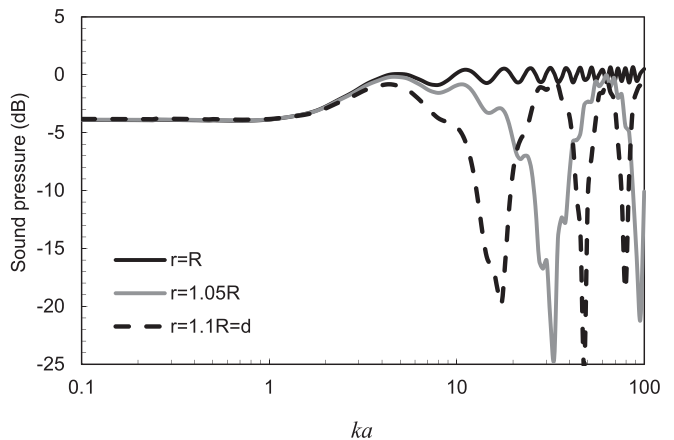

FIG. 4. On-axis near-field pressure due to scattering of resilient disk by a sphere at different positions in gap between them, where both have the same diameters, and the gap is one-twentieth of the diameter of the sphere.

J. Acoust. Soc. Am. **151** (6), June 2022
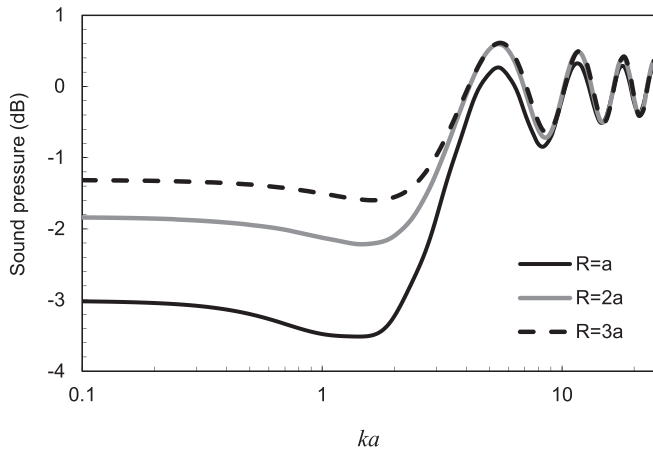
Tim Mellow and Leo Kärkkäinen   4117

FIG. 5. On-axis pressure due to scattering of resilient disk by a sphere with different diameter ratios and no gap between them. Pressure is on surface of sphere and at center of disk.

the center of the disk (dashed black trace). Figure 5 shows the pressure at the center of the disk with no gap, so that it is also the pressure on the surface of the sphere, with different ratios of sphere to disk diameter ranging from unity (solid black) to 3 (dashed black). Figure 6 represents the pressure on the sphere due to a typical headphone, where the diameter of the sphere is three times that of the disk, with different gaps ranging from zero (dashed black) to one-twentieth of the sphere diameter (solid black). We see that the fluctuation of pressure with frequency increases as the gap is increased.

It is also apparent that because the resilient disk is a pressure transducer, it is not reliant on being sealed to the head like a conventional velocity (rigid) transducer to achieve a good low-frequency response. However, the resonance frequency of the flexible diaphragm must be tuned to the lowest frequency of its working range. The pressure field between the resilient disk and sphere is shown for $ka = 20$ in Fig. 7 with $d = R = a$, as shown in Fig. 1.

C. Far-field pressure of the resilient disk
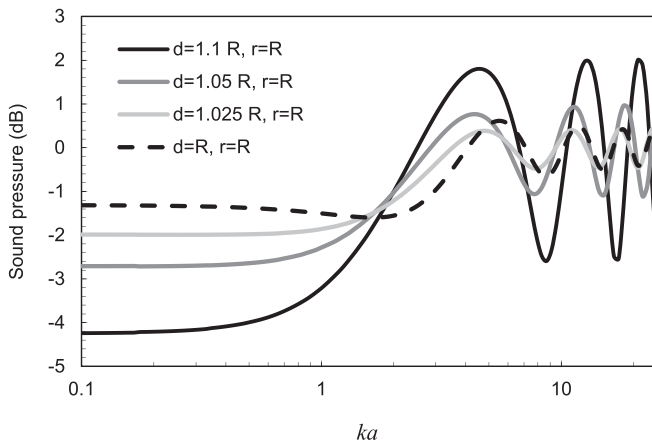
In the far field we have

FIG. 6. On-axis pressure due to scattering of resilient disk by a sphere with different gaps between them, where the diameter of the sphere is three times that of the disk. Pressure is on surface of sphere.
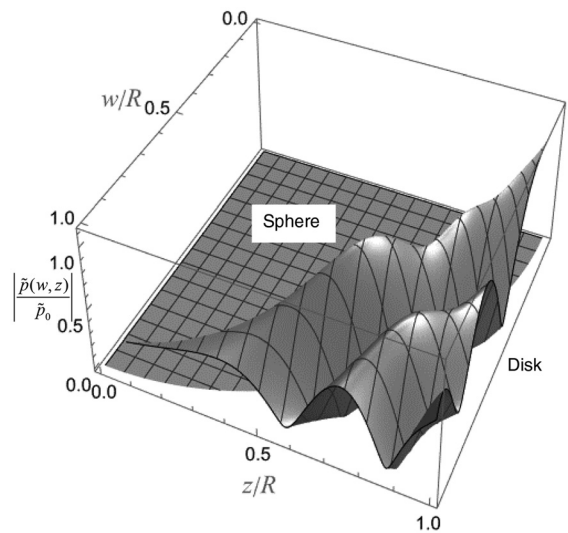
FIG. 7. Pressure field between a *resilient* disk and a rigid sphere for $ka = 20$ with $d = R = a$, as shown in Fig. 1.

$$h_n^{(2)}(kr)\big|_{r\to\infty} = \frac{i^{n+1}}{kr}e^{-ikr}, \tag{25}$$

so that Eq. (22) becomes

$$\tilde{p}(r, \theta) = ika^2 \tilde{p}_0 \frac{e^{-ikr}}{4r} D(\theta), \tag{26}$$

where

$$D(\theta) = \frac{2}{ka} \sum_{n=0}^{\infty} I_n^+(ka) P_n(\cos\theta). \tag{27}$$

Directivity patterns $20\log_{10}|ka\, D(\theta)|$ are plotted in Fig. 8. At very low frequencies, sound diffracts around the sphere, and we see a dipole (or figure-8) pattern as if the sphere
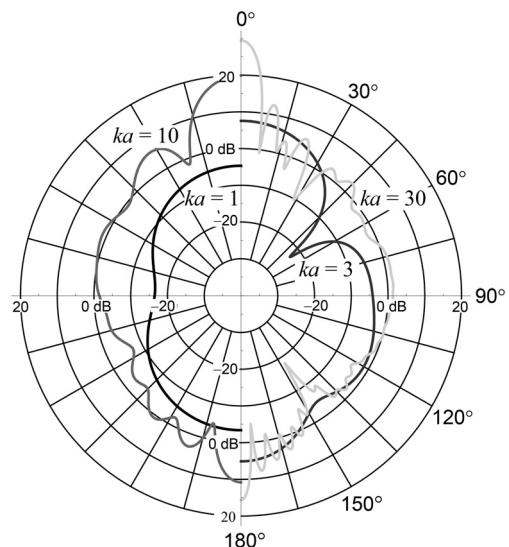

FIG. 8. Resultant far-field directivity patterns of a *resilient* disk scattered by a rigid sphere for various values of ka with $d = R = a$, as shown in Fig. 1.

were not present. However, at the highest frequencies, the pattern becomes increasingly omnidirectional, albeit with a number of narrow nulls and an increasing but narrowing on-axis lobe. The latter is mainly due to the direct sound from the disk. For comparison, Fig. 9 shows the directivity patterns of the resilient disk in the absence of the sphere, where

$$D(\theta) = \frac{2J_1(ka\sin\theta)}{ka\sin\theta}\cos\theta. \tag{28}$$

The sphere clearly has a dramatic effect in widening the pattern at the higher frequencies. Figure 10 shows $20\log_{10}|ka\ D(\theta)|$ plotted against ka for $\theta = 0$ (dashed gray), $\pi/4$ (solid gray), $\pi/2$ (solid black), $3\pi/4$ (solid light gray), and π (dashed black) with $d = R = a$. If the disk is mounted horizontally with the sphere either above or below it, then the black curve roughly represents the sound heard by the listener in the horizontal direction. Above $ka = 2$, this curve is fairly flat, but, not surprisingly, it falls off sharply at lower frequencies because this is the "dead zone" of the dipole pattern. The other two curves rise with increasing frequency due to the formation of lobes at each end of the pattern. However, these lobes also decrease in width and therefore become an ever-smaller portion of the otherwise omnidirectional pattern. The directivity index (DI) is given by

$$DI = 10\log_{10}\left(\frac{2|D(\pi/2)|^2}{\int_0^\pi |D(\theta)|^2\sin\theta d\theta}\right), \tag{29}$$

where we apply the integral identity

$$\int_0^\pi P_m(\cos\theta)P_n(\cos\theta)\sin\theta d\theta = \begin{cases} 0, & m \neq n \\ \dfrac{2}{2n+1}, & m = n \end{cases} \tag{30}$$

to obtain

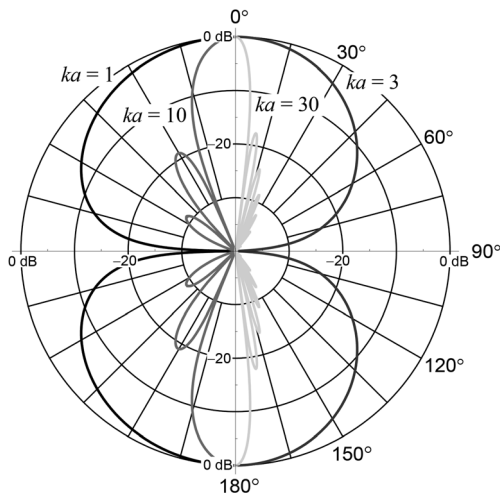$$\int_0^\pi |D(\theta)|^2\sin\theta d\theta = 8\sum_{n=0}^\infty \frac{I_n^+(ka)I_n^{+*}(ka)}{2n+1}. \tag{31}$$

FIG. 9. Far-field directivity patterns of a *resilient* disk in the absence of a sphere for various values of ka.
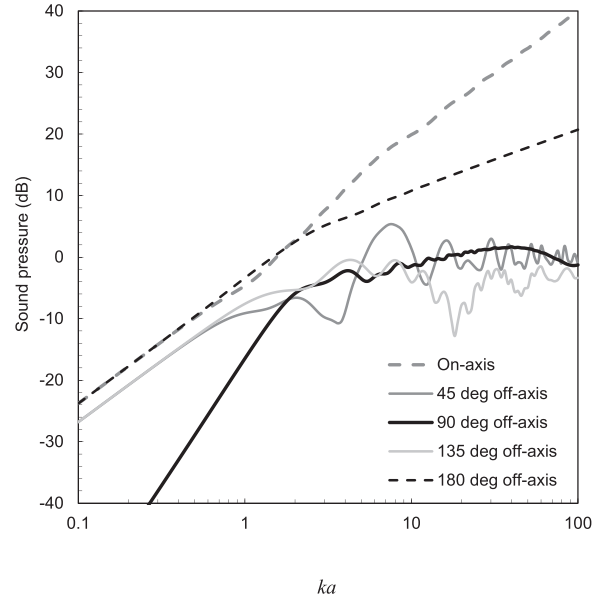
FIG. 10. Resultant far-field sound pressure of a *resilient* disk scattered by a rigid sphere on-axis (dashed gray), 45° off-axis (solid gray), 90° off-axis (solid black), 135° off-axis (solid light gray), and 180° off-axis (dashed black) with $d = R = a$, as shown in Fig. 1.

V. RIGID DISK

A. Calculation of the near-field pressure for the rigid disk

The near-field pressure due to the rigid disk, which is a monopole velocity source, is given by the monopole Rayleigh integral[10]

$$\tilde{p}(r,\theta) = i2k\rho_0 c\tilde{u}_0 \int_0^{2\pi}\int_0^a G(r,\theta|r_0,\theta_0)\Big|_{\substack{r_0=\sqrt{w_0^2+d^2} \\ \cos\theta_0=d/r_0}} w_0 dw_0 d\phi_0. \tag{32}$$

Letting $w_0 = \sqrt{r_0^2 - d^2}$ and $r_0 = at$ in Eq. (25) yields

$$\tilde{p}(r,\theta)$$
$$= k^2 a^2 \rho_0 c\tilde{u}_0 \sum_{n=0}^\infty i^{-n} P_n(\cos\theta)$$
$$\times \begin{cases} I_n^+(ka)h_n^{(2)}(kr), & r > \sqrt{a^2+d^2} \\ I_n^-(ka)\left(j_n(kr) - \dfrac{j'_n(kR)}{h'^{(2)}_n(kR)}h_n^{(2)}(kr)\right), & r \leq \sqrt{a^2+d^2}, \end{cases} \tag{33}$$

where

$$I_n^+(ka) = i^n(2n+1)\int_{d/a}^{\sqrt{1+d^2/a^2}}\left(j_n(kat) - \frac{j'_n(kR)}{h'^{(2)}_n(kR)}h_n^{(2)}(kat)\right)$$
$$\times P_n\left(\frac{d}{at}\right)tdt, \tag{34}$$

$$I_n^-(ka) = i^n(2n+1)\int_{d/a}^{\sqrt{1+d^2/a^2}} h_n^{(2)}(kat)P_n\left(\frac{d}{at}\right)tdt. \tag{35}$$

Again, applying the identities of Eqs. (A12)–(A16) yields

$$I_n^+(ka) = i^n\frac{\sqrt{\pi}}{4}\sum_{m=0}^{\lfloor n/2\rfloor}\frac{(-1)^m(2n+1)\Gamma\left(n-m+\frac{1}{2}\right)}{m!\,\Gamma\left(\frac{n}{2}-m+\frac{1}{2}\right)\Gamma\left(\frac{n}{2}-m+1\right)}\left(\frac{d}{a}\right)^{n-2m}\left\{\left(1-\frac{j'_n(kR)}{h'^{(2)}_n(kR)}\right)\right.$$
$$\times\left(\frac{ka}{2}\right)^n\left(\left(1+\frac{d^2}{a^2}\right)^{m+1}f_n^m\left(-\frac{k^2(d^2+a^2)}{4}\right)-\left(\frac{d}{a}\right)^{2(m+1)}f_n^m\left(-\frac{k^2d^2}{4}\right)\right)+i\frac{j'_n(kR)}{h'^{(2)}_n(kR)}$$
$$\times\left.\left(\frac{-2}{ka}\right)^{n+1}\left(\left(1+\frac{d^2}{a^2}\right)^{m-n+(1/2)}g_n^m\left(-\frac{k^2(d^2+a^2)}{4}\right)-\left(\frac{d}{a}\right)^{2m-2n+1}g_n^m\left(-\frac{k^2d^2}{4}\right)\right)\right\}, \tag{36}$$

$$I_n^-(ka) = i^n\frac{\sqrt{\pi}}{4}\sum_{m=0}^{\lfloor n/2\rfloor}\frac{(-1)^m(2n+1)\Gamma\left(n-m+\frac{1}{2}\right)}{m!\,\Gamma\left(\frac{n}{2}-m+\frac{1}{2}\right)\Gamma\left(\frac{n}{2}-m+1\right)}\left(\frac{d}{a}\right)^{n-2m}$$
$$\times\left\{\left(\frac{ka}{2}\right)^n\left(\left(1+\frac{d^2}{a^2}\right)^{m+1}f_n^m\left(-\frac{k^2(d^2+a^2)}{4}\right)-\left(\frac{d}{a}\right)^{2(m+1)}f_n^m\left(-\frac{k^2d^2}{4}\right)\right)\right.$$
$$-i\left.\left(\frac{-2}{ka}\right)^{n+1}\left(\left(1+\frac{d^2}{a^2}\right)^{m-n+(1/2)}g_n^m\left(-\frac{k^2(d^2+a^2)}{4}\right)-\left(\frac{d}{a}\right)^{2m-2n+1}g_n^m\left(-\frac{k^2d^2}{4}\right)\right)\right\}, \tag{37}$$

where

$$f_n^m(x) = \frac{{}_1F_2\left(m+1;m+2,n+\frac{3}{2};x\right)}{(m+1)\Gamma\left(n+\frac{3}{2}\right)}, \tag{38}$$

$$g_n^m(x) = \frac{{}_1F_2\left(m-n+\frac{1}{2};m-n+\frac{3}{2},\frac{1}{2}-n;x\right)}{\left(m-n+\frac{1}{2}\right)\Gamma\left(\frac{1}{2}-n\right)}. \tag{39}$$

The pressure field between the rigid disk and sphere is shown for $ka=20$ in Fig. 11 with $d=R=a$, as shown in Fig. 1.

B. Far-field pressure of the rigid disk

Again, applying the identity of Eq. (25) yields

$$\tilde{p}(r,\theta) = ika^2\rho_0c\tilde{u}_0\frac{e^{-ikr}}{2r}D(\theta), \tag{40}$$

where

$$D(\theta) = 2\sum_{n=0}^{\infty}I_n^+(ka)P_n(\cos\theta). \tag{41}$$

Directivity patterns $20\log_{10}|ka\,D(\theta)|$ are plotted in Fig. 12. We see that, unlike the resilient disk, which transitions from a dipole at very low frequencies to omnidirectional at higher frequencies, the rigid disk pattern remains largely omnidirectional at all frequencies. For comparison, Fig. 13 shows
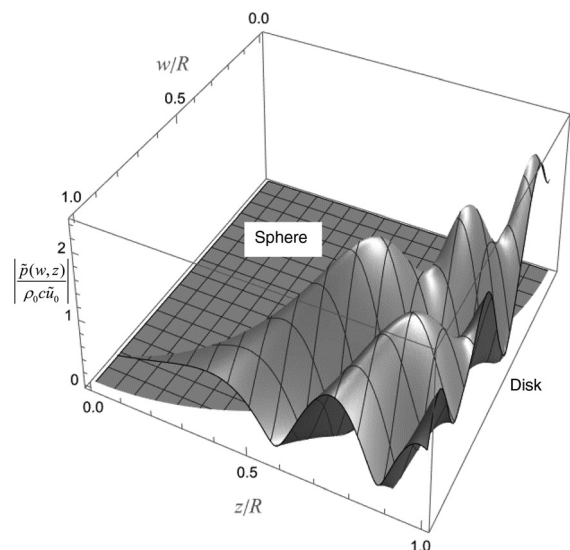

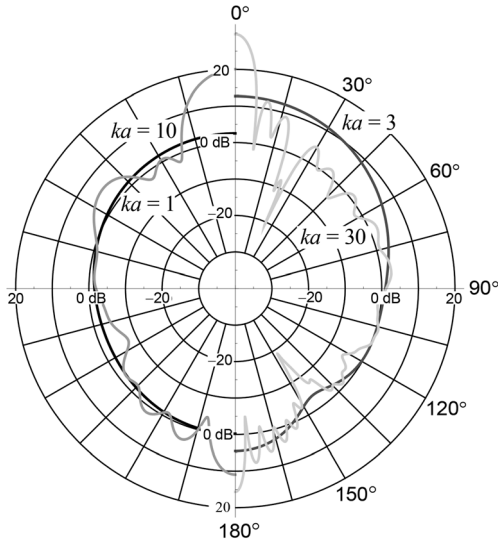FIG. 11. Pressure field between a *rigid* disk and a rigid sphere for $ka=20$ with $d=R=a$, as shown in Fig. 1.

Tim Mellow and Leo Kärkkäinen

FIG. 12. Resultant far-field directivity patterns of a *rigid* disk scattered by a rigid sphere for various values of ka with $d = R = a$, as shown in Fig. 1.

the directivity patterns of the rigid disk in the absence of the sphere, where

$$D(\theta) = \frac{2J_1(ka\sin\theta)}{ka\sin\theta}. \qquad (42)$$

The sphere clearly has a dramatic effect in widening the pattern at the higher frequencies. Figure 14 shows $20\log_{10}|ka\,D(\theta)|$ plotted against ka for $\theta = 0$ (dashed gray), $\pi/4$ (solid gray), $\pi/2$ (solid black), $3\pi/4$ (solid light gray), and π (dashed black) with $d = R = a$. The black curve for the 90° off-axis sound is significantly less regular than that for the resilient disk due to the rigid disk being a reflective surface rather than acoustically transparent like the resilient disk. The effects of these reflections are visible as extra ripples in the near-field pressure plot of Fig. 11 compared to Fig. 7. As with the resilient disk, we see the formation of lobes on-axis and 180° off-axis that produce the rising black and gray
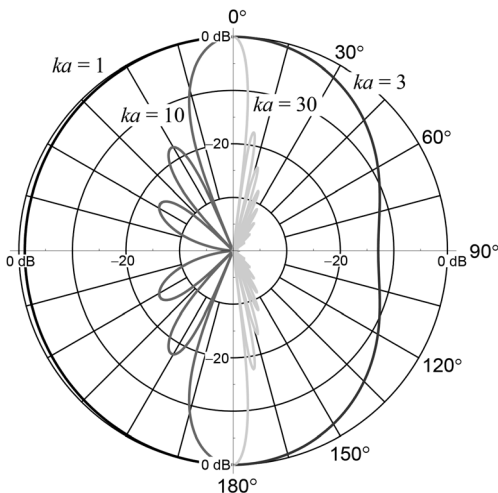

FIG. 13. Far-field directivity patterns of a *rigid* disk in the absence of a sphere for various values of ka.
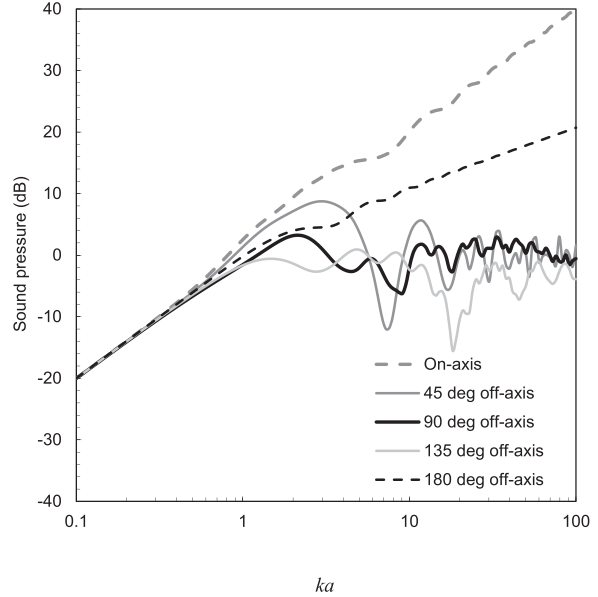

FIG. 14. Resultant far-field sound pressure of a *rigid* disk with constant velocity scattered by a rigid sphere on-axis (dashed gray), 45° off-axis (solid gray), 90° off-axis (solid black), 135° off-axis (solid light gray), and 180° off-axis (dashed black) with $d = R = a$, as shown in Fig. 1.

dashed curves, respectively. Again, the DI is given by Eq. (29) except in this instance,

$$\int_0^\pi |D(\theta)|^2 \sin\theta d\theta = 8ka \sum_{n=0}^{\infty} \frac{I_n^+(ka)I_n^{+*}(ka)}{2n+1}. \qquad (43)$$

DIs are shown in Table I. Apart from at the lowest frequency, where the resilient disk converges to a dipole figure-8 pattern, the resilient disk has a lower DI than the rigid disk at all other frequencies, which verifies that its pattern is closer to omnidirectional.

C. Radiation impedance

The normalized radiation impedance may be found by integrating the near-field pressure over the surface of the disk and dividing this by the product of the disk volume velocity and specific acoustic impedance of free space,

$$Z_R = R_R + iX_R = \frac{1}{\rho_0 c \tilde{u}_0} \int_0^{2\pi} \int_0^a \tilde{p}(r,\theta) \bigg|_{\substack{r=\sqrt{w^2+d^2}\\ \cos\theta=d/r}} w\,dw\,d\phi. \qquad (44)$$

Using the same substitutions and identities as before yields

TABLE I. DIs of the resilient and rigid disks scattered by a sphere.

ka	DI resilient disk (dB)	DI rigid disk (dB)
1	-7.1	-1.2
3	-2.4	-4.4
10	-4.0	-4.8
30	-1.5	-1.9

J. Acoust. Soc. Am. **151** (6), June 2022

Tim Mellow and Leo Kärkäinen   4121

$$Z_R = \frac{\sqrt{\pi}}{4} k^2 a^2 \sum_{n=0}^{\infty} i^{-n} I_{n-}$$

$$\times \sum_{p=0}^{\lfloor n/2 \rfloor} \frac{(-1)^p \Gamma\left(n - p + \frac{1}{2}\right)}{p! \Gamma\left(\frac{n}{2} - p + \frac{1}{2}\right) \Gamma\left(\frac{n}{2} - p + 1\right)} \left(\frac{d}{a}\right)^{n-2p}$$

$$\times \left\{ \left(1 - \frac{j'_n(kR)}{h'^{(2)}_n(kR)}\right) \left(\frac{ka}{2}\right)^n \left(\left(1 + \frac{d^2}{a^2}\right)^{p+1}\right.\right.$$

$$\times f_n^p\left(-\frac{k^2(d^2 + a^2)}{4}\right) - \left(\frac{d}{a}\right)^{2(p+1)} f_n^p\left(-\frac{k^2 d^2}{4}\right)\right)$$

$$+ i \frac{j'_n(kR)}{h'^{(2)}_n(kR)} \left(\frac{-2}{ka}\right)^{n+1} \left(\left(1 + \frac{d^2}{a^2}\right)^{p-n+(1/2)}\right.$$

$$\times g_n^p\left(-\frac{k^2(d^2 + a^2)}{4}\right) - \left(\frac{d}{a}\right)^{2p-2n+1}$$

$$\left.\left.\times g_n^p\left(-\frac{k^2 d^2}{4}\right)\right)\right\}, \tag{45}$$

which is plotted in Fig. 15 for $d = R = a$.

VI. CONCLUSION

We have shown that the rigid sphere is an effective form for broadening the directivity pattern of the sound produced by a planar disk through both simple ray tracing and a more rigorous analysis. It turns out that the resilient disk, which is acoustically transparent, produces a smoother off-axis response than a rigid disk, which itself is a scattering object. One could also investigate the effect of varying the size of the sphere as well as its distance from the disk to see if optimum configurations could be achieved for different situations. For example, could an optimum response be realized for a particular listening position? Or could a more diffuse sound field be created to serve many positions with multiple room reflections creating a live sense of ambience? The latter tuning could be associated with the genre of
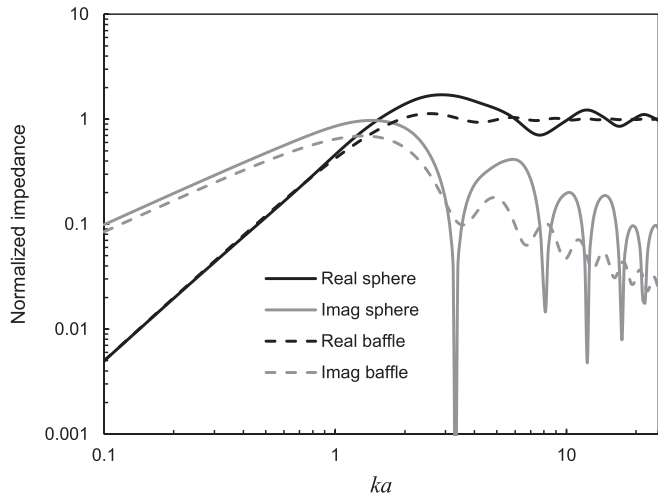

FIG. 15. Real (black solid) and imaginary (gray solid) parts of the normalized radiation impedance Z_R of the rigid disk and sphere with $d = R = a$, as shown in Fig. 1. Also shown, for comparison, are the real (dashed black) and imaginary (dashed gray) parts of the radiation impedance of a rigid disk in an infinite baffle.

music being played. As a bonus, the resilient disk forms an approximate model for a headphone with an electrostatic or planar magnetic transducer.

APPENDIX

We split the integrals I_n^+ and I_n^- of Eqs. (23) and (24), respectively, each into eight parts,

$$I_n^+(ka) = i^{n-1} \left(1 - \frac{j'_n(kR)}{h'^{(2)}_n(kR)}\right) (I_{1n}(ka) - I_{2n}(ka)$$

$$- I_{3n}(ka) + I_{4n}(ka)) + i^n \frac{j'_n(kR)}{h'^{(2)}_n(kR)} (I_{5n}(ka)$$

$$- I_{6n}(ka) - I_{7n}(ka) + I_{8n}(ka)), \tag{A1}$$

$$I_n^-(ka) = i^{n-1} (I_{1n}(ka) - I_{2n}(ka) - I_{3n}(ka) + I_{4n}(ka))$$

$$- i^n (I_{5n}(ka) - I_{6n}(ka) - I_{7n}(ka) + I_{8n}(ka)), \tag{A2}$$

where

$$I_{1n}(ka) = nkd \int_{d/a}^{\sqrt{1 + d^2/a^2}} j_{n-1}(kat) P_n\left(\frac{d}{at}\right) dt$$

$$= \frac{\sqrt{\pi}}{2} \left(\frac{ka}{2}\right)^n n \left\{ \frac{(d/a)^{n+1}}{\Gamma\left(\frac{n+1}{2}\right) \Gamma\left(\frac{n}{2} + 1\right)} \left(\ln\left(1 + \frac{a^2}{d^2}\right) + \frac{k^2 a^2}{2(2n+1)} \left(\frac{d^2}{a^2} {}_2F_3\left(1, 1; 2, 2, n + \frac{3}{2}; -\frac{k^2 d^2}{4}\right)\right.\right.$$

$$\left.\left.- \left(1 + \frac{d^2}{a^2}\right) {}_2F_3\left(1, 1; 2, 2, n + \frac{3}{2}; -\frac{k^2(d^2 + a^2)}{4}\right)\right)\right) + \sum_{m=1}^{n/2} \frac{(-1)^m \Gamma\left(n - m + \frac{1}{2}\right) (d/a)^{n-2m+1}}{m! \Gamma\left(\frac{n}{2} - m + \frac{1}{2}\right) \Gamma\left(\frac{n}{2} - m + 1\right)}$$

$$\times \left(\left(1 + \frac{d^2}{a^2}\right)^m f\left(m, n + \frac{1}{2}, -\frac{k^2(d^2 + a^2)}{4}\right) - \frac{d^{2m}}{a^{2m}} f\left(m, n + \frac{1}{2}, -\frac{k^2 d^2}{4}\right)\right)\right\}, \tag{A3}$$

Tim Mellow and Leo Kärkkäinen

$$I_{2n}(ka) = (n+1)kd \int_{d/a}^{\sqrt{1+d^2/a^2}} j_{n+1}(kat) P_n\left(\frac{d}{at}\right) dt$$

$$= \frac{\sqrt{\pi}}{2}\left(\frac{ka}{2}\right)^{n+2}(n+1)\sum_{m=0}^{n/2}\frac{(-1)^m \Gamma\left(n-m+\frac{1}{2}\right)(d/a)^{n-2m+1}}{m!\,\Gamma\left(\frac{n}{2}-m+\frac{1}{2}\right)\Gamma\left(\frac{n}{2}-m+1\right)}$$

$$\times\left(\left(1+\frac{d^2}{a^2}\right)^{m+1}f\left(m+1,n+\frac{5}{2},-\frac{k^2(d^2+a^2)}{4}\right)-\frac{d^{2m+2}}{a^{2m+2}}f\left(m+1,n+\frac{5}{2},-\frac{k^2d^2}{4}\right)\right),\qquad\text{(A4)}$$

$$I_{3n}(ka) = n(n+1)\int_{d/a}^{\sqrt{1+d^2/a^2}} j_n(kat) P_{n+1}\left(\frac{d}{at}\right) dt$$

$$= \frac{\sqrt{\pi}}{4}\left(\frac{ka}{2}\right)^n n(n+1)\left\{\frac{(d/a)^{n+1}}{\Gamma\left(\frac{n}{2}+1\right)\Gamma\left(\frac{n}{2}+\frac{3}{2}\right)}\left(\ln\left(1+\frac{a^2}{d^2}\right)+\frac{k^2a^2}{2(2n+3)}\right.\right.$$

$$\times\left.\left(\frac{d^2}{a^2}{}_2F_3\left(1,1;2,2,n+\frac{5}{2};-\frac{k^2d^2}{4}\right)-\left(1+\frac{d^2}{a^2}\right){}_2F_3\left(1,1;2,2,n+\frac{5}{2};-\frac{k^2(d^2+a^2)}{4}\right)\right)\right)$$

$$+\sum_{m=1}^{n/2}\frac{(-1)^m\Gamma\left(n-m+\frac{3}{2}\right)(d/a)^{n-2m+1}}{m!\,\Gamma\left(\frac{n}{2}-m+1\right)\Gamma\left(\frac{n}{2}-m+\frac{3}{2}\right)}\left(\left(1+\frac{d^2}{a^2}\right)^m f\left(m,n+\frac{3}{2},-\frac{k^2(d^2+a^2)}{4}\right)-\frac{d^{2m}}{a^{2m}}f\left(m,n+\frac{3}{2},-\frac{k^2d^2}{4}\right)\right)\Bigg\},$$

$$\text{(A5)}$$

$$I_{4n}(ka) = n(n+1)\int_{d/a}^{\sqrt{1+d^2/a^2}} j_n(kat) P_{n-1}\left(\frac{d}{at}\right) dt$$

$$= \frac{\sqrt{\pi}}{4}\left(\frac{ka}{2}\right)^n n(n+1)\sum_{m=0}^{(n-1)/2}\frac{(-1)^m\Gamma\left(n-m-\frac{1}{2}\right)(d/a)^{n-2m-1}}{m!\,\Gamma\left(\frac{n}{2}-m\right)\Gamma\left(\frac{n}{2}-m+\frac{1}{2}\right)}$$

$$\times\left(\left(1+\frac{d^2}{a^2}\right)^{m+1}f\left(m+1,n+\frac{3}{2},-\frac{k^2(d^2+a^2)}{4}\right)-\frac{d^{2m+2}}{a^{2m+2}}f\left(m+1,n+\frac{3}{2},-\frac{k^2d^2}{4}\right)\right),\qquad\text{(A6)}$$

$$I_{5n}(ka) = nkd\int_{d/a}^{\sqrt{1+d^2/a^2}} y_{n-1}(kat) P_n\left(\frac{d}{at}\right) dt$$

$$= \frac{\sqrt{\pi}}{2}\left(\frac{2}{ka}\right)^{n-1}n\sum_{m=0}^{n/2}\frac{(-1)^{m+n}\Gamma\left(n-m+\frac{1}{2}\right)(d/a)^{n-2m+1}}{m!\,\Gamma\left(\frac{n}{2}-m+\frac{1}{2}\right)\Gamma\left(\frac{n}{2}-m+1\right)}\left(\left(1+\frac{d^2}{a^2}\right)^{m-n+(1/2)}f\left(m-n+\frac{1}{2},\frac{3}{2}-n,-\frac{k^2(d^2+a^2)}{4}\right)\right.$$

$$\left.-\frac{d^{2m-2n+1}}{a^{2m-2n+1}}f\left(m-n+\frac{1}{2},\frac{3}{2}-n,-\frac{k^2d^2}{4}\right)\right),\qquad\text{(A7)}$$

$$I_{6n}(ka) = (n+1)kd\int_{d/a}^{\sqrt{1+d^2/a^2}} y_{n+1}(kat) P_n\left(\frac{d}{at}\right) dt$$

$$= \frac{\sqrt{\pi}}{2}\left(\frac{2}{ka}\right)^{n+1}(n+1)\sum_{m=0}^{n/2}\frac{(-1)^{m+n}\Gamma\left(n-m+\frac{1}{2}\right)(d/a)^{n-2m+1}}{m!\,\Gamma\left(\frac{n}{2}-m+\frac{1}{2}\right)\Gamma\left(\frac{n}{2}-m+1\right)}\left(\left(1+\frac{d^2}{a^2}\right)^{m-n+(1/2)}\right.$$

$$\times f\left(m-n+\frac{1}{2},-\frac{1}{2}-n,-\frac{k^2(d^2+a^2)}{4}\right)-\frac{d^{2m-2n+1}}{a^{2m-2n+1}}f\left(m-n+\frac{1}{2},-\frac{1}{2}-n,-\frac{k^2d^2}{4}\right)\right),\qquad\text{(A8)}$$

$$I_{7n}(ka) = n(n+1)\int_{d/a}^{\sqrt{1+d^2/a^2}} y_n(kat)P_{n+1}\left(\frac{d}{at}\right)dt$$

$$= \frac{\sqrt{\pi}}{4}\left(\frac{2}{ka}\right)^{n+1} n \sum_{m=0}^{(n+1)/2} \frac{(-1)^{m+n+1}\Gamma\left(n-m+\frac{3}{2}\right)(d/a)^{n-2m+1}}{m!\,\Gamma\left(\frac{n}{2}-m+1\right)\Gamma\left(\frac{n}{2}-m+\frac{3}{2}\right)}\left(\left(1+\frac{d^2}{a^2}\right)^{m-n-(1/2)}\right.$$

$$\times f\left(m-n-\frac{1}{2},\frac{1}{2}-n,-\frac{k^2(d^2+a^2)}{4}\right) - \frac{d^{2m-2n-1}}{a^{2m-2n-1}}f\left(m-n-\frac{1}{2},\frac{1}{2}-n,-\frac{k^2d^2}{4}\right)\Bigg), \tag{A9}$$

$$I_{8n}(ka) = n(n+1)\int_{d/a}^{\sqrt{1+d^2/a^2}} y_n(kat)P_{n-1}\left(\frac{d}{at}\right)dt$$

$$= \frac{\sqrt{\pi}}{4}\left(\frac{2}{ka}\right)^{n+1} n(n+1) \sum_{m=0}^{(n-1)/2} \frac{(-1)^{m+n+1}\Gamma\left(n-m+\frac{1}{2}\right)(d/a)^{n-2m-1}}{m!\,\Gamma\left(\frac{n}{2}-m\right)\Gamma\left(\frac{n}{2}-m+\frac{1}{2}\right)}\left(\left(1+\frac{d^2}{a^2}\right)^{m-n+(1/2)}\right.$$

$$\times f\left(m-n+\frac{1}{2},\frac{1}{2}-n,-\frac{k^2(d^2+a^2)}{4}\right) - \frac{d^{2m-2n+1}}{a^{2m-2n+1}}f\left(m-n+\frac{1}{2},\frac{1}{2}-n,-\frac{k^2d^2}{4}\right)\Bigg), \tag{A10}$$

where

$$f(\mu,\nu,z) = \frac{{}_1F_2(\mu;\mu+1,\nu;z)}{\mu\Gamma(\nu)}, \tag{A11}$$

${}_1F_2$ is the hypergeometric function, and we have used the integral identities[15]

$$\int j_n(kat)t^\gamma dt = \frac{\sqrt{\pi}}{2}\left(\frac{ka}{2}\right)^n \frac{{}_1F_2\left(\frac{n+\gamma+1}{2};\frac{n+\gamma+3}{2},n+\frac{3}{2};-\frac{k^2a^2t^2}{4}\right)}{(n+\gamma+1)\Gamma\left(n+\frac{3}{2}\right)} t^{n+\gamma+1}, \tag{A12}$$

$$\int y_n(kat)t^\gamma dt = \frac{\sqrt{\pi}}{2}\left(\frac{-2}{ka}\right)^{n+1} \frac{{}_1F_2\left(\frac{\gamma-n}{2};\frac{\gamma-n}{2}+1,\frac{1}{2}-n;-\frac{k^2a^2t^2}{4}\right)}{(\gamma-n)\Gamma\left(\frac{1}{2}-n\right)} t^{\gamma-n}, \tag{A13}$$

together with

$$P_n^m(z) = \left(-2\sqrt{z^{-2}-1}\right)^m \sum_{k=0}^{\lfloor(n-m)/2\rfloor} \frac{(-1)^k\Gamma\left(n-k+\frac{1}{2}\right)}{k!\,\Gamma\left(\frac{n-m}{2}-k+\frac{1}{2}\right)\Gamma\left(\frac{n-m}{2}-k+1\right)} z^{n-2k}, \tag{A14}$$

$$j_n(z) = \frac{\sqrt{\pi}}{2}\sum_{l=0}^{\infty} \frac{(-1)^l}{l!\,\Gamma\left(l+n+\frac{3}{2}\right)}\left(\frac{z}{2}\right)^{2l+n}, \tag{A15}$$

$$y_n(z) = \frac{\sqrt{\pi}}{2}\sum_{l=0}^{\infty} \frac{(-1)^{l+n+1}}{l!\,\Gamma\left(l-n+\frac{1}{2}\right)}\left(\frac{z}{2}\right)^{2l-n-1}. \tag{A16}$$

$$\Gamma(m)\left(\left(1+\frac{d^2}{a^2}\right)^m - \frac{d^{2m}}{a^{2m}}\right)_{m\to 0} = \ln\left(1+\frac{a^2}{d^2}\right). \tag{A17}$$

Equations (A3) and (A5) for I_{1n} and I_{3n}, respectively, have singularities in the expression of Eq. (A11) for f when $m=0$. Therefore, we must expand the hypergeometric functions and find the limit of the first term as $m \to 0$ using

[1]F. E. Toole, "Music, rooms and listeners: Science in the creation and delivery of audio art," Acoust. Today **9**(2), 36–44 (2013).
[2]S. Linkwitz, "The magic in 2-channel sound reproduction—Why is it so rarely heard?," Int. J. Archit. Eng. Technol. **2**, 113-126 (2015).
[3]J. Watkinson, "We need to talk about SPEAKERS: Sorry, 'audiophiles,' only IT will break the sound barrier: Design, DSPs and the debunking of traditional hi-fi," http://www.theregister.co.uk/2014/07/02/feature_the_future_loudspeaker_design/?page=1 (Last viewed June 13, 2022).
[4]H. Haas, "The influence of a single echo on the audibility of speech," J. Audio Eng. Soc. **20**(2), 146–159 (1972).
[5]W. H. Idling, "Unidirectionally radiating loudspeakers," in *Proceedings of the 72nd Convention of the Audio Engineering Society*, Munich, Germany (March 14–16, 1972).

[6]H. F. Olson, "Gradient loudspeakers," J. Audio Eng. Soc. **21**(2), 86–93 (1973).

[7]J. Valin, "Jürgen Reis: A man for all seasons," https://www.theabsolute sound.com/articles/the-absolute-sounds-high-end-audio-hall-of-fame-2020-inductees (Last viewed June 13, 2022).

[8]B. Fox, "Technology: Speakers beam out stereo sound to a wider audience," https://www.newscientist.com/article/mg13017744-800-technology-speake rs-beam-out-stereo-sound-to-a-wider-audience/ (Last viewed June 13, 2022).

[9]P. J. Walker, "New developments in electrostatic loudspeakers," J. Audio Eng. Soc. **28**(11), 795–799 (1980).

[10]L. L. Beranek and T. J. Mellow, *Acoustics: Sound Fields, Transducers, and Vibration*, 2nd ed. (Academic, London, 2019), pp. 560–566, 607, Eq. (13.6), 608, Eq. (13.15), 798–801.

[11]N. A. Gumerov and R. Duraiswami, "Modeling the effect of a nearby boundary on the HRTF," in *Proceedings of the 2001 IEEE International Conference on Acoustics, Speech, and Signal Processing*, Salt Lake City, UT (May 7–11, 2001), Vol. 5, pp. 3337–3340.

[12]R. O. Duda and W. L. Martens, "Range dependence of the response of a spherical head model," J. Acoust. Soc. Am. **104**(5), 3048–3058 (1998).

[13]S. C. Hawkins, T. Rother, and J. Wauer, "A numerical study of acoustic scattering by Janus spheres," J. Acoust. Soc. Am. **147**(6), 4097–4105 (2020).

[14]J. Zhong, R. Kirby, M. Karimi, H. Zou, and X. Qiu, "Scattering by a rigid sphere of audio sound generated by a parametric array loudspeaker," J. Acoust. Soc. Am. **151**(3), 1615–1626 (2022).

[15]I. S. Gradshteyn and I. M. Ryzhik, *Table of Integrals, Series, and Products*, 6th ed., edited by A. Jeffrey (Academic, New York, 2000), p. 960, Eq. (8.772.1).